Journal of Nuclear Medicine, published on June 21, 2019 as doi:10.2967/jnumed.119.229997

PennPET Explorer: Design and Preliminary Performance of a Whole-body Imager

Joel S. Karp[1], Varsha Viswanath[2], Michael J. Geagan[1], Gerd Muehllehner[3], Austin R. Pantel[1], Michael J. Parma[1], Amy E. Perkins[4], Jeffrey P. Schmall[1], Matthew E. Werner[1], Margaret E. Daube-Witherspoon[1]

[1] Department of Radiology, University of Pennsylvania, Philadelphia, PA
[2] Department of Biomedical Engineering, University of Pennsylvania, Philadelphia, PA
[3] KAGE Medical, Wayne, PA
[4] Philips Healthcare, Highland Heights, OH

Financial support:

We acknowledge support from NIH R01-CA206187, R33-CA225310 and R01-CA113941. We also acknowledge support from Philips Healthcare and the Department of Radiology, University of Pennsylvania.

Author responsible for correspondence:

Joel S. Karp, Ph.D.
3620 Hamilton Walk, 154 John Morgan Building
University of Pennsylvania
Philadelphia, PA 19104
(215) 573-4998
fax: (215) 573-3880
joelkarp@pennmedicine.upenn.edu

Total # words: 6778

Running title: PennPET Explorer design and performance

ABSTRACT: We report on the development of the PennPET Explorer whole-body imager. **Methods:** The PennPET Explorer is a multi-ring system designed with a long axial field-of-view (AFOV). The imager is scalable and comprises multiple 22.9-cm long ring-segments, each with 18 detector modules based on the digital Philips Digital Photon Counting (PDPC) silicon photomultiplier. A prototype three-segment imager has been completed and tested with an active 64-cm AFOV. **Results:** The instrument design is described, and its physical performance measurements are presented. These include sensitivity of 55 kcps/MBq, spatial resolution of 4.0 mm, energy resolution of 12%, timing resolution of 250 ps, and a noise equivalent count rate above 1000 kcps beyond 30 kBq/cc. Following an evaluation of lesion torso phantoms to characterize the imager's quantitative accuracy, human studies were performed on normal volunteers. **Conclusion:** The physical performance measurements validate the system design and lead to the high quality human studies. A more detailed examination of human imaging with this whole-body imager is presented in a companion paper.

Key words: Positron Emission Tomography, whole-body imager, NEMA performance

INTRODUCTION

In the last two decades, commercial PET scanner performance has improved dramatically with CT-based attenuation correction (*1*), the use of LSO or LYSO scintillators (*2-3*), time-of-flight (TOF) reconstruction (*4-7*), and most recently silicon photomultiplier (SiPM)-based TOF detectors (*8-9*). However, the axial field-of-view (AFOV) has not grown; it remains 16-26 cm for the newest commercial SiPM-based scanners (*10-12*). This choice is due mainly to scintillator and (SiPM) photosensor costs, and the prevalence of clinical ^{18}F-fluorodeoxyglucose (FDG) scanning focused on measuring lesion standardized uptake value (SUV), typically at 60 minutes post-injection (p.i.) when the uptake is assumed to be at steady-state. The newest commercial instruments perform an FDG whole-body survey ('eyes-to-thighs') with excellent diagnostic quality in 10-20 minutes using bed translation. The motivation for a long-AFOV PET system is to use its high sensitivity to enhance clinical performance and to enable research applications requiring simultaneous measurement of multiple organ systems (*13*). It is unknown whether such a system would primarily be used clinically to take advantage of high throughput and/or low-dose imaging or for research with new radiotracers. We developed the PennPET Explorer whole-body imager to support both clinical and research applications.

The performance benefits of a long-AFOV scanner have been simulated (*14-15*). A few such systems have been built (*16-18*) but have not transitioned to clinical or research use. That is expected to change with the introduction of the uEXPLORER from United Imaging Healthcare (UIH). Developed for UC Davis as part of the EXPLORER Consortium (*19*) the uEXPLORER has a 195-cm AFOV, allowing single-position total-body imaging (*20*) with high sensitivity from head to foot. The EXPLORER Consortium also supported the development of our system, which we describe as a whole-body imager, since it does not require multi-position scanning nor does it cover the total body, as with the UIH instrument. The general design of the prototype was described earlier (*21-22*) as a 3-ring, 70-cm AFOV system. The system is operational with

an active 64-cm AFOV, long enough to demonstrate the merits of simultaneous head and torso imaging. A system of this length also has high sensitivity and can perform very short scans with high quality. In addition, the prototype configuration has enabled us to address the major technical and scientific challenges of designing a long-AFOV instrument. The challenges include i) acquiring and processing very high-throughput data sets, ii) reconstructing quantitative images with minimal image quality losses from degrading effects, such as axial parallax from oblique lines-of-response (LORs), and iii) maintaining reliability as ring-segments are added. The prototype evaluated here has three ring-segments, but the design can be expanded easily. We believe that the optimal axial length of a whole-body imager is in the range of 1.0 to 1.4 meter, and that the clinical and research benefits will justify the increased system cost and complexity.

The PennPET Explorer is described in the next section, followed by the data acquisition methods. We then present measurements quantifying the physical system performance, along with phantom and initial human images demonstrating its imaging performance.

MATERIALS and METHODS

Design of the PennPET Explorer: The basic building block of the PennPET Explorer is a detector tile of 64 lutetium-yttrium oxyorthosilicate (LYSO) scintillation crystals, which is currently used in the Philips *Vereos* PET/CT scanner (*10*). The 8x8 array of 3.86x3.86x19-mm^3 crystals is coupled to a digital silicon photomultiplier (dSiPM) developed by Philips Digital Photon Counting (PDPC) (*23*-*24*). The dSiPM sensor tile is fully digital with 64 individual devices per dSiPM. This true 1:1 crystal-sensor coupling leads to nearly ideal crystal identification, high countrate capability, and superior timing resolution. The detector module design allows close ring spacing and operation at 5˚C with the first photon trigger level setting (*25*) to optimize the timing resolution. The entire gantry and its associated electronics are water-cooled; a chiller is used to cool facility water to ~0˚C to achieve 5˚C at the sensor with less than 1˚C variation over

the full system. Condensation is prevented by infusion of dry purge air to the scanner. In contrast, the same devices in the Philips *Vereos* PET/CT (*10*) operate at 18˚C and at a higher trigger level.

Each ring-segment measures 76.4-cm in diameter and 22.9 cm axially, comprising 18 modules of 28 detector tiles in a 4x7 array. The PennPET Explorer is fully sealed and maintains its own cool, dry environment independent of ambient conditions. The ring-segments are mounted on linear rails to allow for service access and system expansion. The prototype configuration described in this paper consists of 3 ring-segments (**Fig. 1**).

Data Acquisition: The data acquisition system utilizes the Philips *Vereos* electronic components and collects data as singles events. A master clock distributed to all rings was implemented to eliminate inter-ring timing skew. Data (8 bytes/event) are buffered to independent solid-state drive (SSD) arrays on each ring-segment at rates up to 100 Mcps, then merged in near real-time into a single stream of time-sorted data. Since each ring operates autonomously, the multi-ring system maintains high throughput, independent of the number of ring-segments. This results in low deadtime, a key requirement for dynamic imaging where the full tracer bolus will be in the FOV after injection. Following acquisition, the singles data are sorted off-line at a rate of 3 B events/min (with 16-core Intel® Xeon® Processor) into coincidence list files of prompt and delayed events. A typical human study leads to 20 to 200 B events, based on initial FDG studies, e.g., a 10-min static (1 hr p.i.) vs. a 60-min dynamic study; thus, the processing time is similar to the acquisition time. Although the singles list file is large, the sorted coincidence list file is 10-20x smaller and can easily be archived.

Sensor Calibration: Tile sensors require calibration for consistent energy, timing, crystal, and detector identification encoded for each event. The PennPET Explorer calibrations are based on the PDPC sensors' calibrations (*23*), with run time reduced to about 1 hour for parallel (all rings)

calibration. In brief, the dSiPM sensor is first calibrated for the PDE (photo detection efficiency) and TDC (timing digital conversion), and an inhibit map is applied to selectively turn off noisy micro-cells within the digital device. Then a point source centered in the field-of-view is used to calculate the energy and timing for each module, and offset values are calculated for each crystal and stored in the module's on-board memory. The calibrations are stable over many months and are typically needed only after detector module replacement.

While the data acquisition and calibrations are based on the 16.4-cm AFOV Philips *Vereos*, we have expanded the ring-segment's axial length to 22.9 cm by adding two rows of tile detectors to each module. Read-out of these additional rows required a firmware change that had not been implemented when data were collected for this paper; therefore, these data include gaps of 7.4 cm between the ring-segments and an active AFOV of 64 rather than 70 cm. See illustration of detector geometry in supplemental **Fig. 1.**

Data Correction and Image Generation: The data correction and image generation methods have been translated from previous work. The scatter correction method was adapted from the TOF-enhanced single-scatter-simulation method (*26-27*). With a long AFOV scanner the effects of scatter from out-of-field activity are less significant.

We modified the detector efficiency normalization method to accommodate the long AFOV. Previously, a 20-cm diameter uniform cylinder was used; however, when extended to 1 meter or longer, such a phantom is unwieldly and maintaining activity uniformity is difficult. Instead, normalization data are acquired with a thin steel tube filled with ~70 MBq ^{18}F centered in a thin-walled, 1"-diameter carbon fiber tube with negligible attenuation that provides rigidity over the 70-cm length. Using an asynchronous motor mounted to the back plate of the gantry the line rotates at 2 rpm, at a radius just outside the transverse FOV, and data are acquired for about 1

hour for an integer number of rotations to collect a sufficient number of counts for all LORs. This method can be extended to a longer AFOV by increasing the carbon fiber tube diameter but maintaining the same wall thickness. Normalization correction factors are generated by calculating the ratio of the collected data to an analytical rotating line sinogram, followed by modest 'Casey' smoothing (*28*).

Phantom and human data were reconstructed using the TOF list-mode (LM) ordered subsets expectation maximization (OSEM) (*29*) algorithm (25 subsets, 4 iterations) into 2-mm isotropic voxels. This algorithm includes 'blob' basis functions optimized in size and grid spacing for the spatial resolution and noise characteristics of the imager (*30*). These basis functions suppress image noise while preserving signal, hence no post-filtering is needed.

Our data format supports a 5-ns maximum coincidence window (8 bits, 19.5 ps time bins), and we set the transverse FOV to 57.6 cm. The PennPET Explorer in its current geometry has a maximum axial acceptance angle of $\pm 40^{\circ}$ in the center of the AFOV. The large acceptance angle is not limited in any of the studies presented and leads to the high sensitivity and gain in image signal-to-noise; however, for a typical human body the most oblique LORs are attenuated (*31*). Thus, for human studies it will be attenuation of the oblique LORs that limits the gain in image signal-to-noise, rather than the axial acceptance angle or the coincidence window.

Performance Characterization:

Performance measurements were taken on the prototype 3-segment system to optimize the hardware and software for acquisition and reconstruction and to demonstrate the PennPET Explorer's capabilities. The inter-segment gaps halve the sensitivity and reduce the AFOV from 70 cm to 64 cm. These restrictions did not prevent us from achieving our goals: to demonstrate both technical design and imaging performance of the whole-body PET imager. For all NEMA

performance studies and for phantom and human studies we used an energy window of 440-660 keV and a coincidence window of 4 ns. All phantom measurements used ^{18}F activity, except for the spatial resolution measurements that used the sealed ^{22}Na source.

NEMA measures: NEMA NU-2 (*32*) measurements of i) sensitivity, ii) count-rate performance, iii) timing resolution, and iv) spatial resolution were performed. The sensitivity measurement was performed at 2 positions (r = 0 and 10 cm) with a 70-cm long line source inside a set of aluminum tubes. The count-rate measurement was performed with a 70-cm long line source offset inside a 20-cm diameter polyethylene scatter cylinder, at an initial activity concentration of ~40 kBq/cc. The count-rate data were also used for measuring the timing resolution as a function of activity. Spatial resolution was measured using a 0.5-mm diameter ^{22}Na point source encased in a 1-cm^3 plastic cube, imaged at multiple radial positions (1, 5, 10, 15, and 20 cm) and at multiple axial locations (0, 4, 12, 20, 24, 28 cm) relative to the AFOV center. Per NEMA, single-ring data were reconstructed using the analytic DIRECT algorithm (*33*). We also report the results from LM-OSEM iterative reconstruction for single-ring and 3-ring data, using parameters optimized for high-resolution imaging (1-mm^3 voxels, 4 iterations). While this may not yield an absolute measure of spatial resolution for a point source in air, the results provide insight into the dependence of spatial resolution on the axial acceptance angle as it increases toward the mid-AFOV.

Phantom measures: (A) The NEMA image quality (IQ) phantom was filled per the harmonization initiative (*34*). This measurement is similar to NEMA, but uses a different body activity concentration and sphere contrast – 2 kBq/ml and 9.7:1. All spheres were hot (per the NU-2 2018 update) with a cold, lung-like region in the center. The NEMA IQ phantom was positioned with the spheres centered axially. The phantom was imaged with the standard NEMA spheres (diameters from 10, 13, 17, 22, 28, 37 mm) and with a second set of half-sized spheres (8.5,

11.5, 15, 19, 25, 32, 44 mm) developed by the harmonization initiative to facilitate matching the contrast recovery coefficient (CRC) curves between scanners. The phantom was imaged with each set of spheres for 30 min (per harmonization instructions), and the list-mode data were sub-sampled into scans as short as 1 min. The CRC was calculated using circular regions of interest (ROIs) with diameters equal to the sphere inner diameters, per NEMA NU-2.

(B) The SNMMI Clinical Trials Network (CTN) lesion phantom (*35*) has a similar range of lesion sizes as the NEMA IQ phantom, although its 30-cm axial length still falls short of that needed to measure long-AFOV system performance. The phantom was filled with an activity concentration of 5.9 kBq/ml and a lesion contrast ratio of 4.2:1. The phantom was roughly centered in the AFOV and imaged for 60 min so the data could be sub-sampled to shorter scans of 6 min to 15 s, with 10 replicates per scan duration. CRCs were determined for the 10 to 28-mm diameter spheres.

Human studies: In the evaluation of a new instrument, human studies are crucial to establish the real-world performance beyond phantom studies and to test and optimize data acquisition and reconstruction. A Penn research protocol allows human imaging on the PennPET Explorer. The study has been approved by the University of Pennsylvania Institutional Review Board, and all subjects signed an informed consent form. We have completed ten human studies, and a more detailed examination of human imaging, including clinical patients, will be presented in a companion paper. Three studies involving normal volunteers are shown here: two static and one dynamic. Subject #1 (F, 62 y.o., BMI = 26.5, 163 cm) was injected with 555 MBq FDG in the clinic, scanned on the clinical Philips Ingenuity TF PET/CT at about 1 hr p.i., then imaged at 1.5 hr p.i. at a single bed position on the PennPET Explorer for 20 min, the same time as the clinical scan. The full data set was sub-sampled and reconstructed to emulate shorter scans, or lower dose. With subject #2 (F, 56 y.o., BMI = 21.6, 155 cm), the brain was first imaged near the end

of the AFOV and then centered in the AFOV, where the sensitivity is higher but axial parallax errors increase. FDG uptake in the cortical grey matter in the brain provides a good opportunity to evaluate complex structure and the effect of reconstructed spatial resolution. In the third study presented, subject #7 (F, 29 y.o., BMI = 19.3, 177 cm) was injected with a fast bolus (~ 2 s) inside the PennPET Explorer and imaged for a full hour to capture the early kinetics of FDG for all organ systems simultaneously. Attenuation correction for these studies was done using the CT scan from the Philips Ingenuity TF PET/CT with rigid-body registration (MIM Software, Inc., Cleveland, OH) applied to the preliminary non-attenuation corrected PennPET Explorer images. To aid in the alignment both patient couches had affixed a flat pallet with cushions set with indexing marks so as to position the subjects in a similar manner.

RESULTS

Sensitivity: The total sensitivity of the 3 ring-segment PennPET Explorer is 54 kcps/MBq at r=0 cm and 57 kcps/MBq at r=10 cm. While the sensitivity is much higher than that of commercial instruments, we note that the data gaps in the prototype lead to a 2x reduction in sensitivity. Normalization correction compensates for these axial sensitivity variations and a demonstration of the uniformity of a reconstructed long cylinder of activity is shown in Supplemental **Fig. 1.** The excellent image uniformity is a key to achieving quantitative accuracy with phantom and human studies.

Count-rate: The count-rate performance is shown in **Fig. 2.** These results demonstrate that the trues rate is linear over a very wide range of activity, up to 38 kBq/cc - about 10x that of a clinical FDG study. The calculated scatter fraction is 32% and is stable over this range of activity. The noise equivalent count rate (NECR) continues to increase slowly beyond the point at which trues = randoms (at 15 kBq/cc) reaching 1050 kcps at 38 kBq/cc.

Timing resolution: At low activity, the full-system timing resolution is 256 ps, increasing linearly to 284 ps at the highest activity. For individual ring-segments, the average timing resolution is 249±6 ps at low activity, increasing to 263±5 ps at the highest activity. Thus, the loss due to oblique LORs in the 3-ring system is modest. There is also close agreement (at low rates) with bench-top timing measurements of 240 ps for individual PDPC tiles, implying little loss of performance in translating from single detectors to complete, fully calibrated rings.

Spatial resolution: **Table 1** summarizes the spatial resolution results**,** while more detailed plots are shown in Supplemental **Fig. 2.** Transverse results are averages over all axial source positions at that radial position; axial results are averages over all transverse source positions, and the uncertainties shown are the standard deviations over the different source positions. Analytic DIRECT reconstruction was performed with data from a single ring-segment; the spatial resolution (full-width-at-half-maximum, FWHM) in the center of the transverse FOV is ~4.0 mm (transverse and axial), with an expected loss of radial resolution at increased radii. The full-width-at-tenth-maximum (FWTM) in the center of the transverse FOV is 8.0-8.5 mm. Spatial resolution results are also shown for LM-OSEM using all data from 1 and 3 ring-segments (axial acceptance angle from ±8˚ to ±40˚). Although the absolute values of FWHM can depend on the number of iterations, it is important to note that the LM-OSEM transverse resolution results were very similar to those from analytic reconstruction. These results also demonstrate only a small dependence of axial resolution on the axial acceptance angle and on axial location.

Image quality phantom: The NEMA IQ phantom was acquired sequentially with the standard set of spheres, followed by the half-size set of spheres. In both cases, the spheres were centered axially. The results in **Fig. 3** demonstrate the value of having smaller spheres where the CRC changes rapidly with diameter and, therefore, will be more sensitive to the choice of

reconstruction parameters. Also shown is the background variability for several scan durations. For the current 64-cm AFOV, the updated NEMA prescription suggests a scan duration of ~10 min (scan time = axialstep x 30 min/100 cm) using ½ AFOV (32 cm) for axialstep to achieve a total-body scan of 100 cm in 30 min. Because the phantom was filled per the harmonization initiative, the activity concentration was ~2 kBq/ml (0.05 μCi/ml), lower than that prescribed by NEMA (5.2 kBq/ml or 0.14 μCi/ml). Thus, these scan times should be scaled for comparison with NEMA results.

CTN lesion phantom: **Fig. 4 (a)** shows typical CTN phantom images for 6- and 1-min acquisitions. CRC as a function of scan duration is shown for different sphere sizes in **Fig. 4 (b)**; CRCs are stable to 60 s (or less), with precision of ≤10% SD of the CRC mean for scans shorter than 120 s (**Fig. 5 (c)**). These results predict good quantitative accuracy for human studies with shorter scan times than used in clinical practice.

Human studies: The image from the full 20-min scan of subject #1 is shown in **Fig. 5,** along with a scan subsampled to represent a 2.5-min scan and the 20-min scan (2 min/bed x 10 beds) from the clinical scanner. For this comparison, the clinical data were reprocessed using the same reconstruction tools as the PennPET data, although for routine clinical diagnostics, the clinical data are reconstructed with a smoother basis function and into 4-mm^3 voxels, rather than the 2-mm^3 voxels shown here.

Fig. 6 shows 10-min images of the brain acquired sequentially at 2 axial locations, starting at 1.5 hr p.i. Predictably, the image acquired near the edge of the AFOV (top) has approximately 50% of the counts of the image acquired near the center of the AFOV (bottom); however, it is difficult to see spatial resolution degradation for the brain in the center of the AFOV despite the larger axial acceptance angle.

Fig. 7 shows representative time frames for subject #7 during the initial uptake, starting with 1-s frames following injection, as well as the final (5-min) frame at 55-60 min. These images demonstrate the enormous potential of dynamic imaging with a large AFOV that includes both brain and torso and with the ability to measure the blood input function and multi-organ kinetics. The singles rate at bolus injection (40 Mcps/ring) is in the range of linear behavior and well below our maximum data rate; thus we can accurately model the tracer behavior.

DISCUSSION

In this paper, we described the design of the PennPET Explorer and evaluated its performance in its prototype, 3-ring configuration. We focused on tests and metrics that help characterize and illustrate its behavior, particularly in areas that are influenced by the large AFOV compared to existing systems.

We presented a representative set of NEMA tests to characterize the prototype's performance, including sensitivity, spatial resolution, count-rate, and timing resolution measurements. A more complete set of NEMA tests will be performed after the prototype transitions to its final configuration. It is convenient that the prescribed 70-cm long sensitivity and count-rate phantoms of the NU-2 standard are still applicable for the 64-cm prototype, but some of these measurements may need revision once the imager is extended past 70 cm. The measured sensitivity is very high at 55 kcps/MBq, about 9x that of a single ring, even with data gaps of ~30% of the ring-segment axial length.

The count-rate capability is typically characterized by the peak NECR, but we did not reach the peak even at 38 kBq/cc - well beyond expected human protocol rates even with short-lived isotopes (e.g., ^{11}C). It may be more relevant to cite the NECR at 1/10 that activity: 290 kcps at 3.8 kBq/cc. Notably, the true coincident event rate is nearly linear over this wide range of

activities. This is a consequence of the single event throughput rate, which reaches 57 Mcps/ring at 38 kBq/cc.

Point source transverse spatial resolution is 4.0 mm (FWHM) near the center (at 1 cm). Radial resolution increases to 5.6 mm at 20 cm. Axial resolution is 4 mm near the center, using data from a single ring, but 3-ring data could not be processed with the analytic algorithm as the gaps result in an incomplete data set. Instead we demonstrated with the LM-OSEM algorithm that there is only a small loss in axial resolution with 3-ring vs. single-ring data. Care must be taken when iteratively reconstructing point sources in air but, as these results were independent of iteration count (4-10 iterations), we believe they represent the behavior of spatial resolution versus location. We also note that simulations modeling a gapless 3-ring geometry (*31, 21*) predicted an axial resolution loss of 0.5 mm with an analytic algorithm, measured at the AFOV center and including all LORs.

The phantom studies demonstrate the system's imaging performance and serve as a precursor to human imaging, since they were used to optimize the acquisition and reconstruction choices. The IQ phantom was imaged per the harmonization initiative and the CRC values fall in line with those of other modern PET/CT scanners (*34*), and importantly those performed on the Philips Vereos (*34*), which uses the same underlying hardware. Predictably, our measured noise levels are lower, as expected for a whole-body imager with a long AFOV. The CTN torso phantom was used to better illustrate the behavior of the long AFOV system, since it is 30 cm in axial length, with lesions throughout the torso region. This phantom demonstrated robust quantitative accuracy for scan durations of 1 min or less with a precision of the CRC measurement of < 10% for scans as short as 2 min.

Performing the first human studies is a critical and exciting step in any new system development, as these studies validate its design and operation. Although the whole-body images from the prototype PennPET Explorer have less axial coverage than the typical 'eyes-to-thighs' whole-body survey, these studies represent the quality achievable with a large AFOV. The human images demonstrate image quality superior to that of a clinical standard-of-care FDG scan. By sub-sampling the list data set, we have also demonstrated excellent image quality that corresponds to significantly shorter scans or lower dose. We also note that these images, acquired with a single bed position, have uniform noise behavior over the entire AFOV, except at the end slices. This is important for an instrument designed as an imager, rather than a scanner requiring bed translation. The dynamic data set presents compelling evidence of how such an instrument can be used to probe multi-organ kinetics, particularly as it achieves excellent image quality with time frames as short as 1 s. The progression of the blood and tracer distribution is clearly demonstrated in the first few minutes of the dynamic study. In our companion paper we present additional human studies to explore further new opportunities with a long AFOV PET imager.

Although the PennPET Explorer was not deliberately designed with inter-ring axial gaps, the images presented were acquired with data gaps between rings. It has been suggested that inter-ring gaps could extend an imager's AFOV (*36*) or allow for imaging during radiation treatment (*37*). Our results shows excellent image quality and uniform quantitative behavior independent of axial location, suggesting that inter-ring gaps are an effective means of increasing the AFOV for a given number of detectors. This is a very important consideration for a whole-body imaging system whose hardware cost is a practical limitation. In addition, system reliability is critical, since a multi-ring system has many individual components. We have paid considerable attention to design robustness and have developed many useful quality control and detector monitoring aids. Our experience with the prototype after close to a year in

operation is that it will be a reliable system even as additional rings are added to expand the AFOV of the whole-body imager. Even so, the impact of localized detector failures will be mitigated by the high amount of redundant data due to the large number of LORs.

CONCLUSION

The three ring-segment prototype PennPET Explorer has been completed and tested. The design of the scalable imaging system was described, and characterization of the instrument and imaging performance was presented. Initial phantom and human studies with the PennPET Explorer demonstrate excellent performance and validate the successful implementation of many key components of the design related to the data acquisition and reconstruction of large data sets in a multi-ring configuration. We plan to integrate the prototype with a CT scanner, and the AFOV will be extended by adding rings to expand the capabilities of this whole-body imager for both clinical and research applications and to accommodate a wider range of human height.

Disclosure: We acknowledge support from NIH R01-CA206187, R33-CA225310 and R01-CA113941. We also acknowledge support from the Department of Radiology, University of Pennsylvania and from Philips Healthcare in a Research Agreement with the University of Pennsylvania. No other potential conflicts of interest relevant to this article exist.

Acknowledgments: We are grateful to Dr. Chi-Hua Tung of Philips Healthcare for his partnership from the onset of this project, and technical support from the Philips CT/AMI R&D group. We are also grateful for ongoing support from the Department of Radiology and the commitment of our chair, Dr. Mitchell Schnall, and our vice-chair, Dr. David Mankoff, to provide funding for instrumentation development and construction of an imaging facility. This scanner could not have been constructed without the expertise and involvement of Tim McDermott for developing manufacturing procedures and assembling the scanner and without help from our student assistants, Timothy McSorley, Joe Shiiba, and Ben Culmer, in the construction of the prototype. We further thank Eric Blankemeyer, Joshua Scheuermann, and Dr. Janet Reddin for assistance with imaging studies, Drs. David Mankoff and Daniel Pryma for guiding the human studies, Erin Schubert for assistance in writing the IRB and coordination with her clinical research team in performing the human studies, and the PET Center Cyclotron facility for providing activity for the phantom studies and radiotracers for the human studies.

Key Points

QUESTION: How does larger axial coverage of a PET instrument lead to improved image quality and affect quantitative accuracy?

PERTINENT FINDINGS: The performance of the prototype configuration of the PennPET Explorer has been tested and the initial phantom and human studies demonstrate excellent image quality. These studies validate the successful implementation of the key components of the design related to the data acquisition and reconstruction of large data sets in a multi-ring configuration.

IMPLICATIONS FOR PATIENT CARE: The high sensitivity and large axial coverage of the PennPET Explorer whole-body imager will lead to benefits for clinical FDG studies and also enable translational research that leverages the ability to measure kinetics in multi-organ systems.

References

(*1*) Kinahan PE, Townsend DW, Beyer T, Sashin D. Attenuation correction for a combined 3D PET/CT scanner. *Med Phys.* 1998;25:2046-2053.

(*2*) Wienhard K, Schmand M, Casey M, et al. The ECAT HRRT: Performance and first clinical application of the new high resolution research tomograph. *IEEE Trans Nucl Sci*. 2002;49:104-10.

(*3*) Spinks TJ, Bloomfield PM. A comparison of count rate performance for 15-O-water blood flow studies in the CTI HR+ and Accel tomographs in 3D mode. In: *Conference Record of the 2002 IEEE Nuclear Science Symposium and Medical Imaging Conference*. Norfolk, VA: IEEE; 2002.

(*4*) Surti S, Karp JS. Advances in time-of-flight PET. *Physica Medica: Eur J Med Phys*. 2016;32:12-22.

(*5*) Conti M. Focus on time-of-flight PET: the benefits of improved time resolution. *Eur J Nucl Med Mol Imag*. 2011;38:1147-57.

(*6*) Lois C, Jakoby BW, Long MJ, et al. An assessment of the impact of incorporating time-of-flight information into clinical PET/CT imaging. *J Nucl Med.* 2010;51:237-245.

(*7*) Karp JS, Surti S, Daube-Witherspoon ME, Muehllehner G. Benefit of time-of-flight in PET: experimental and clinical results. *J Nucl Med.* 2008;49:462-470.

(*8*) Surti S, Karp JS. Advances in time-of-flight PET. *Phys Med Biol*. 2016;32:12-22.

(*9*) Vandenberghe S, Mikhaylova E, D'Hoe E, Mollet P, Karp JS. Recent developments in time-of-flight PET. *Eur J Nucl Med Mol Imaging Phys*. 2016;3:3. https://doi.org/10.1186/s40658-016-0138-3.

(*10*) Rausch I, Ruiz A, Valverde-Pascual I, Cal-Gonzalez J, Beyer T, Carrio I. Performance evaluation of the Vereos PET/CT system according to the NEMA NU2-2012 standard. *J Nucl Med.* 2019;60:561–567.

(*11*) Hsu DFC, Ilan E, Peterson WT, Uribe J, Lubberink M, Levin CS. Studies of a next-generation silicon-photomultiplier-based time-of-flight PET/CT system. *J Nucl Med*. 2017;58:1511-1518.

(*12*) Reddin JS, Scheuermann JS, Bharkhada D, et al. Performance evaluation of the SiPM-based Siemens Biograph Vision PET/CT system. In: *Conference Record of the 2018 IEEE Nuclear Science Symposium and Medical Imaging Conference*. Sydney, AU: IEEE; 2018.

(*13*) Cherry SR, Badawi RD, Karp JS, Moses WW, Price P, Jones T. Total-body imaging: Transforming the role of positron emission tomography. *Sci Transl Med*. 2017;9:381. https://doi.org/10.1126/scitranslmed.aaf6169.

(*14*) Poon JK, Dahlbom ML, Moses WW, et al. Optimal whole-body PET scanner configurations for different volumes of LSO scintillator: a simulation study. *Phys Med Biol.* 2012;57:4077-4094.

(*15*) Surti S, Karp JS. Impact of detector design on imaging performance of a long axial field-of-view, whole-body PET scanner. *Phys Med Biol.* 2105;60:5343–5358.

(*16*) Watanabe M, Shimizu K, Omura T, et al., A high-throughput whole-body PET scanner using flat panel PS-PMTs. *IEEE Trans Nucl Sci*. 2004;51:796-800.

(*17*) Conti M, Bendriem B, Casey M, et al. Performance of a high sensitivity PET scanner based on LSO panel detectors. *IEEE Trans Nucl Sci*. 2006;53:1136-1142.

(*18*) Moskal P, Rundel O, Alfs D, et al. Time resolution of the plastic scintillator strips with matrix photomultiplier readout for J-PET tomograph. *Phys Med Biol*. 2016;61:2025-2047.

(*19*) Cherry SR, Jones T, Karp JS, Qi J, Moses WW, Badawi RD. Total-body PET: Maximizing sensitivity to create new opportunities for clinical research and patient care. *J Nucl Med.* 2018;59:3-12.

(*20*) Badawi RD, Shi H, Hu P, et al. First in human imaging studies with the Explorer total-body PET scanner. *J Nucl Med*. 2019;60:299-303.

(*21*) Viswanath V, Daube-Witherspoon ME, Schmall JP, et al. Development of PET for total-body imaging. *Acta Phys Pol B.* 2017;48:1555-1566.

(*22*) Karp JS, Geagan MJ, Muehllehner G, et al. The PennPET eXL scanner for total body applications. In: *Conference Record of the 2017 IEEE Nuclear Science Symposium and Medical Imaging Conference*. Atlanta, GA: IEEE; 2017.

(*23*) Frach T, Prescher G, Degenhardt C, Gruyter R, Schmitz A, Ballizany R. The digital silicon photomultiplier— principle of operation and intrinsic detector performance. In: *Conference Record of the 2009 IEEE Nuclear Science Symposium and Medical Imaging Conference.* Orlando, FL*: IEEE;* 2009.

(*24*) Degenhardt C, Prescher G, Frach T, et al. The digital silicon photomultiplier – A novel sensor for the detection of scintillation light. In: *Conference Record of the 2009 IEEE Nuclear Science Symposium and Medical Imaging Conference.* Orlando, FL: IEEE; 2009.

(*25*) Schmall JP, Geagan MJ, Werner ME, Parma MJ, Viswanath V, McDermott T, Perkins AE, Karp JS. Characterizing the TOF performance of the PennPET Explorer scanner [abstract]. *J Nucl Med*. 2018:59(suppl 1):96.

(*26*) Accorsi R, Adam LE, Werner ME, Karp JS. Optimization of a fully 3D single scatter simulation for 3D PET. *Phys Med Biol.* 2004;49:2577-2598.

(*27*) Werner ME, Surti S, Karp JS. Implementation and evaluation of a 3D PET single scatter simulation with TOF modeling. In: *Conference record of the 2006 IEEE Nuclear Science Symposium and Medical Imaging Conference*. San Diego, CA: IEEE; 2006.

(*28*) Casey ME, Hoffman EJ. Quantitation in positron emission computed tomography: 7. A technique to reduce noise in accidental coincidence measurements and coincidence efficiency calibration. *J Comput Assist Tomogr.* 1986;10:845-850.

(*29*) Popescu LM, Matej S, Lewitt RM. Iterative image reconstruction using geometrically ordered subsets with list-mode data. In: *Conference Record of the 2004 Nuclear Science Symposium and Medical Imaging Conference*. Rome, Italy: IEEE; 2004.

(*30*) Matej S, Lewitt RM. Practical donsiderations for 3-D image reconstruction using spherically-symmetric volume elements. *IEEE Trans Med Imaging.* 1996;15:68-78.

(*31*) Schmall JP, Werner ME, Surti S. Parallax error in long-axial field-of-view PET scanners – a simulation study. Phys Med Biol. 2016;61:5443-5455.

(*32*) *NEMA Standards Publication NU 2-2018 – Performance Measurements of Positron Emission Tomographs (PET)*. Rosslyn, VA: National Electrical Manufacturers Association; 2018.

(*33*) Matej S, Daube-Witherspoon ME, Karp JS. Analytic TOF PET reconstruction algorithm within DIRECT data partitioning framework. *Phys Med Biol*. 2016;61:3365-3386.

(*34*) Sunderland JJ, Kinahan PE, Karp JS, et al. Development and testing of a formalism to identify harmonized and optimized reconstructions for PET/CT in clinical trials [abstract]. *J Nucl Med*. 2015;56(suppl):563.

(*35*) Sunderland JJ, Christian P. Quantitative PET/CT scanner performance characterization based upon the Clinical Trials Network oncology clinical simulator phantom. *J Nucl Med*. 2015;56:145-52.

(*36*) Wong W-H, Zhang Y, Liu S, et al. The initial design and feasibility study of an affordable high-resolution 100-cm long PET. In: *Conference Record of the 2007 IEEE Nuclear Science Symposium and Medical Imaging Conference*. Honolulu, HI: IEEE; 2007.

(*37*) Yamaya T, Inaniwa T, Minohara S, et al. A proposal of an open PET geometry. *Phys Med Biol.* 2008;53:757-773.

FIGURE 1: PennPET Explorer in its prototype configuration with 3 ring-segments, housed in a dry, cool enclosure. View of the back of the gantry shows modular detector and electronic bays. Also shown is couch with flat pallet installed for human studies.

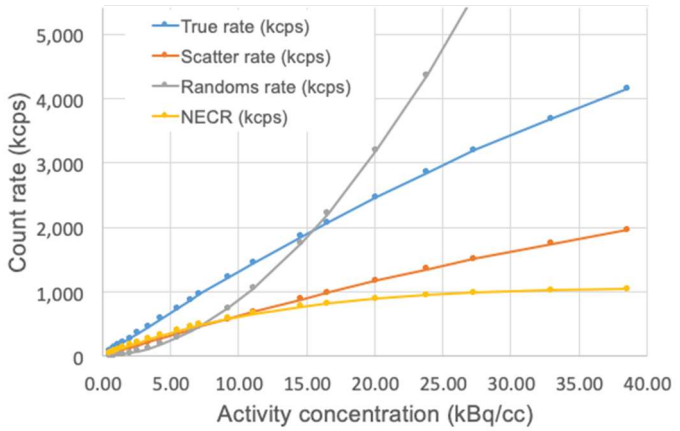

Figure 2: NEMA NU-2 count-rate performance with 70-cm line source inside a 20-cm diameter polyethylene scatter cylinder. Count-rate results acquired up to 40 kBq/cc, although clinical FDG studies are typically performed with activity concentrations < 5 kBq/cc.

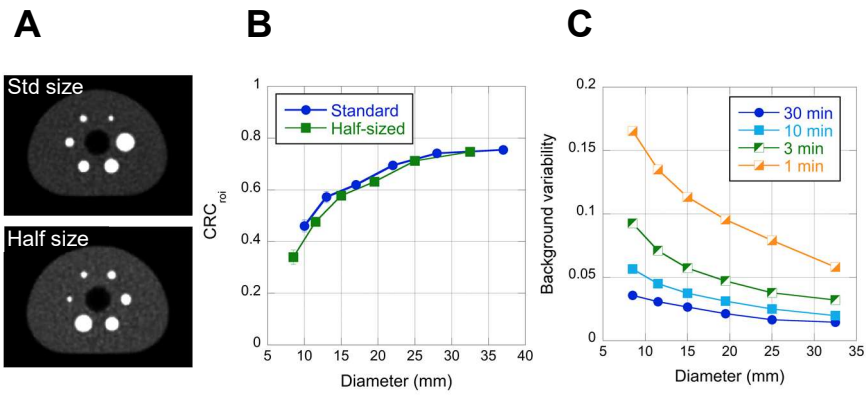

Figure 3: A) NEMA IQ phantom shown with standard spheres (top) and half-sized spheres (bottom). Body activity is 2 kBq/ml, sphere contrast is 9.7:1, and scan duration is 7.5 min. **B)** Contrast recovery coefficients as per NEMA guidelines for both standard and half-sized spheres. **C)** Background variability as per NEMA guidelines for half-sized spheres.

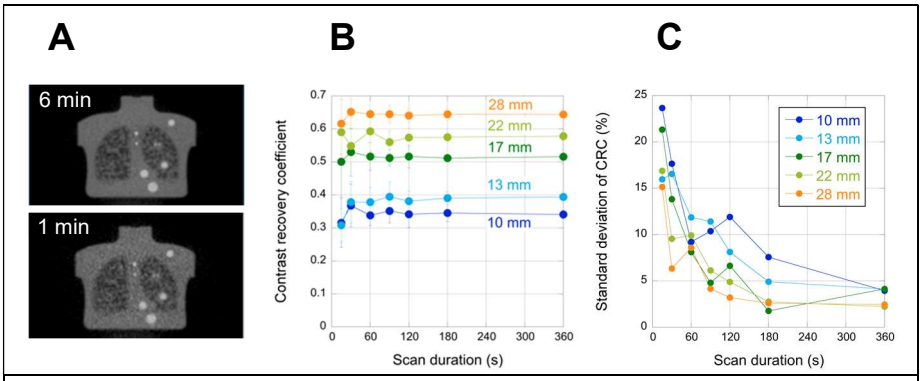

Figure 4: A) CTN torso phantom with activity concentration of 5.9 kBq/ml and lesion contrast of 4.2:1. Top (6 min) and bottom (1 min) scan. **B)** Contrast recovery coefficient of representative lesions as a function of scan duration. **C)** Standard deviation of CRC, determined from replicates of data.

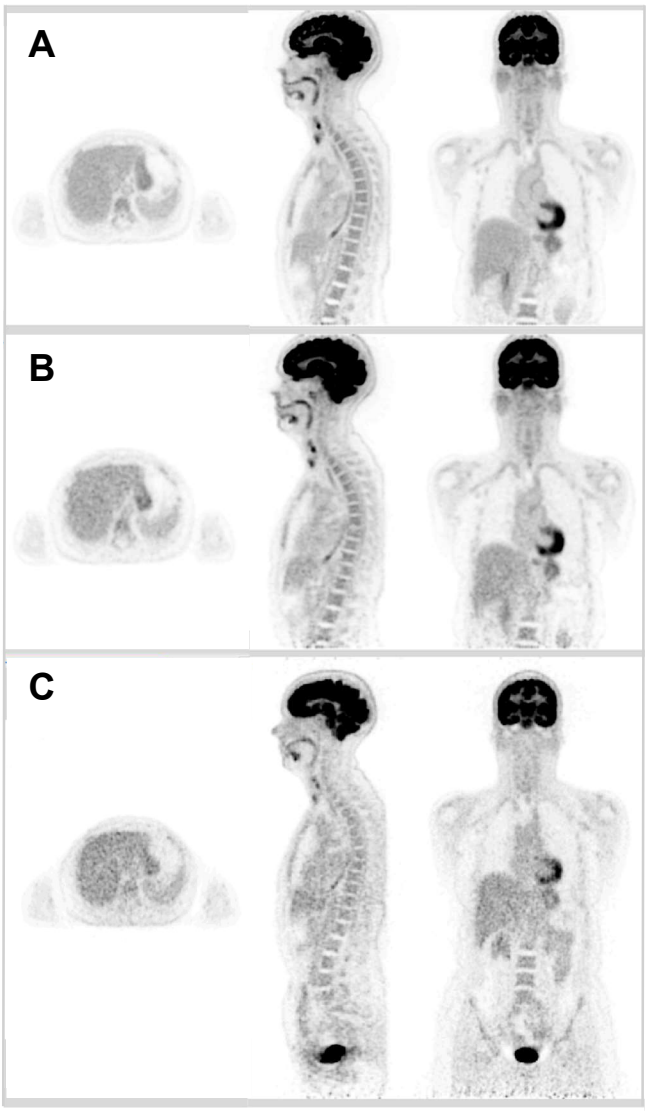

Figure 5: A) Representative views of 20-min PennPET Explorer image of subject #1 at 1.5 hr p.i. following 555 MBq dose of FDG. All 2-mm sections. **B)** PennPET Explorer image, sub-sampled (1/8 data) to represent 2.5 min scan. **C)** Clinical scan with Philips *Ingenuity TF* PET/CT, 1 hr p.i. acquired with clinical protocol, 10 bed positions for total of 20 min. These data were reconstructed off-line with same reconstruction method as the PennPET Explorer data.

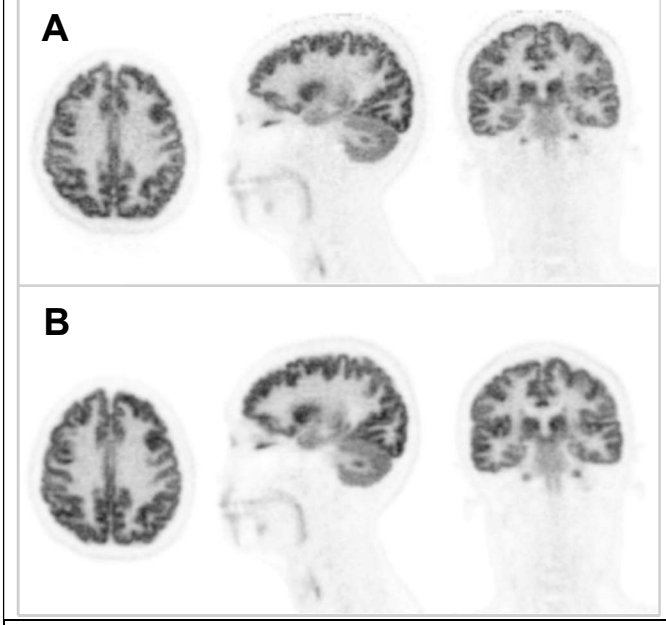

Figure 6: A) Subject #2 positioned with head near the edge of the AFOV and **B)** at the center of the AFOV. These scans were acquired starting at 1.5 hr p.i. for 10-min durations each. All 1-mm sections.

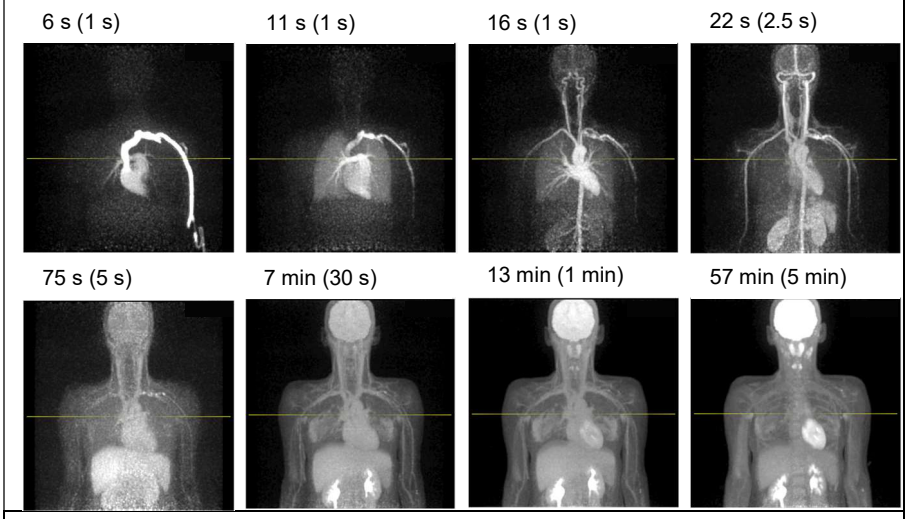

Figure 7: Dynamic FDG study of subject #7 acquired for 60 min following 555 MBq dose. Representative MIP images are shown from 0 to 60 min post-injection.

TABLE 1. Spatial resolution of PennPET Explorer whole-body imager

			FWHM[1] (mm)		
R (cm)	# rings	Algorithm	Radial	Tangential	Axial
1	1	Analytic	4.2 ± 0.3	3.9 ± 0.4	4.1 ± 0.2
1	1	Iterative	3.9 ± 0.3	3.8 ± 0.3	3.6 ± 0.2
1	3	Iterative	3.9 ± 0.2	3.9 ± 0.3	3.9 ± 0.3
10	3	Iterative	4.2 ± 0.2	3.9 ± 0.2	3.9 ± 0.3
20	3	Iterative	5.6 ± 0.2	3.9 ± 0.4	3.7 ± 0.3
			Axial FWHM (mm)		
			Center	Gap	Edge
1-20	1	Iterative	---	---	3.5 ± 0.2
1-20	3	Iterative	4.0 ± 0.2	4.2 ± 0.1	3.6 ± 0.1

			FWTM[2] (mm)		
R (cm)	# rings	Algorithm	Radial	Tangential	Axial
1	1	Analytic	8.5 ± 0.8	8.4 ± 0.9	7.9 ± 0.2
1	1	Iterative	7.2 ± 0.4	7.1 ± 0.2	6.8 ± 0.2
1	3	Iterative	7.4 ± 0.6	7.3 ± 0.2	7.8 ± 1.2
10	3	Iterative	8.1 ± 0.2	7.2 ± 0.2	7.6 ± 0.8
20	3	Iterative	10.4 ± 0.3	7.2 ± 0.2	7.3 ± 0.7
			Axial FWTM (mm)		
			Center	Gap	Edge
1-20	1	Iterative	---	---	6.8 ± 0.1
1-20	3	Iterative	8.5 ± 0.6	8.2 ± 0.1	6.9 ± 0.2

Uncertainties are standard deviations of replicate measurements

[1] Full-width at half-maximum

[2] Full-width at tenth-maximum

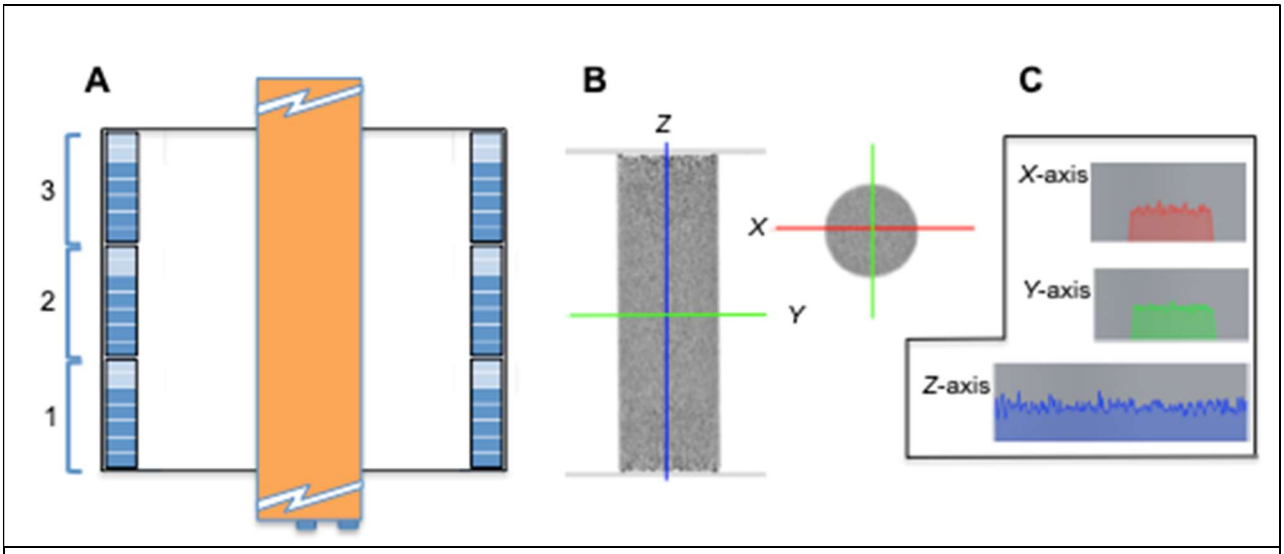

Supplemental Figure 1: A) Schematic of detector geometry for 3 rings, illustrating the active detector (5 rows, dark blue) and inactive detector (2 rows, light blue) for each ring, leading to gaps in collected data. Illustration includes pipe phantom, 20-cm diameter by 1.2 m long. **B)** Axial (sagittal) and transverse images, each 2-mm thick, following a 1-hr scan with 222 MBq (6 mCi) ^{18}F. **C)** Profiles through images in X-Y (transverse) and Z (axial) directions.

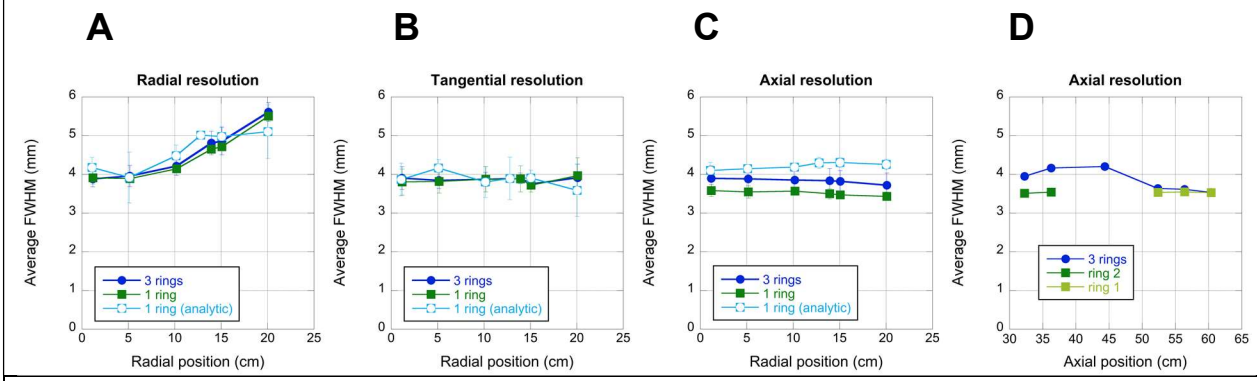

Supplemental Figure 2: A) Radial spatial resolution with analytic DIRECT and iterative LM-OSEM. Analytic results are shown only for a single ring, whereas LM-OSEM results are shown for data from a single ring and all 3 rings together. **B)** Tangential spatial resolution as a function of radial position. **C)** Axial spatial resolution as a function of radial position. **D)** Axial spatial resolution as a function of axial position. Position 32 cm is at the center of the AFOV, 44 cm is in a gap, and 62 cm is near the edge.